IEEE Access
Multidisciplinary | Rapid Review | Open Access Journal

Received 23 June 2025, accepted 7 July 2025, date of publication 16 July 2025, date of current version 22 July 2025.

Digital Object Identifier 10.1109/ACCESS.2025.3589930

RESEARCH ARTICLE

Metal-Stamped and IR-UWB-Optimized Air-Filled Cavity-Backed Antenna Array for Cost-Effective Single-Anchor 3D Localization

GERT-JAN GORDEBEKE, (Member, IEEE), SAM LEMEY, (Member, IEEE), AND HENDRIK ROGIER, (Senior Member, IEEE)

IDLab, Electromagnetics Group, Department of Information Technology, Ghent University-IMEC, 9052 Ghent, Belgium

Corresponding author: Gert-Jan Gordebeke (gertjan.gordebeke@ugent.be)

ABSTRACT A cost-effective, yet high-performance, time-domain-optimized air-filled cavity-backed metal-stamped slot antenna is presented for next-generation multi-channel, multi-antenna IR-UWB applications. Equipping a quarter-mode metal-stamped cavity with a novel feeding mechanism yields a compact $0.43\,\lambda_0 \times 0.43\,\lambda_0$ antenna that is compatible with standard low-cost manufacturing processes and that has a fractional bandwidth of 34.4 %, covering UWB channels 5, 6, 8 and 9. The antenna is optimized in the frequency and time domains for IR-UWB applications. It is robust against variations in material properties and manufacturing inaccuracies in the metal stamping process. Furthermore, it retains its performance when exploited in a three-element V-shaped antenna array for single-anchor distance and 2D angle-of-arrival estimation. Measurements demonstrate excellent estimation performance in both free-space conditions and challenging real-life deployment scenarios. Specifically, 97 % of all distance estimation errors are below 2 cm, with a mean absolute error (MAE) of 7.1 mm. In terms of angle estimation, 91 % of all errors are below 10°, with an MAE of 5.0°. These results highlight the antenna's excellent IR-UWB and isolation performance, enabling single-anchor 3D localization for Industry 4.0 and Healthcare 4.0 applications.

INDEX TERMS Air-filled cavity-backed antenna, angle-of-arrival (AoA) estimation, impulse-radio ultra-wideband (IR-UWB), metal stamping, single-anchor localization, time-domain optimization.

I. INTRODUCTION

The impulse-radio ultra-wideband (IR-UWB) technology has emerged as the prime candidate for positioning systems in challenging environments [1], [2], [3], [4]. By transmitting (sub)nanosecond pulses, centimeter-level accuracy can be reached with high resilience against multipath interference, leading to its adoption in a myriad of applications [4], [5], [6]. Yet, next-generation IR-UWB applications in Industry 4.0 and Healthcare 4.0, such as smart factories, ambient-assisted living, and emergency response coordination [7], [8], [9] (Fig. 1), require multi-antenna nodes to further improve positioning accuracy and reliability while reducing the number of anchor nodes [10], including single-anchor three-dimensional (3D) localization [9], [11], [12], and to implement sensing/radar functionality [13], [14].

Although a plethora of UWB monopole and dipole antennas [14], [15], [16], [17], [18], [19] have been introduced over the years, they suffer from limited isolation and efficiency, performance degradation due to their integration platform [20] and/or suboptimal time-domain performance [21]. Recently, air-filled cavity-backed slot antennas have emerged as a new class of IR-UWB antennas, propelled by their high efficiency [22], [23], excellent robustness against integration platform effects [24] and high isolation in compact array configurations [25]. By exploiting miniaturization techniques [22], [24], compact and wideband air-filled cavity-backed antennas have been realized that are suitable for robust $\lambda/2$-spaced 2D arrays in challenging environments [25]. Furthermore, their performance in the

The associate editor coordinating the review of this manuscript and approving it for publication was Ravi Kumar Gangwar.

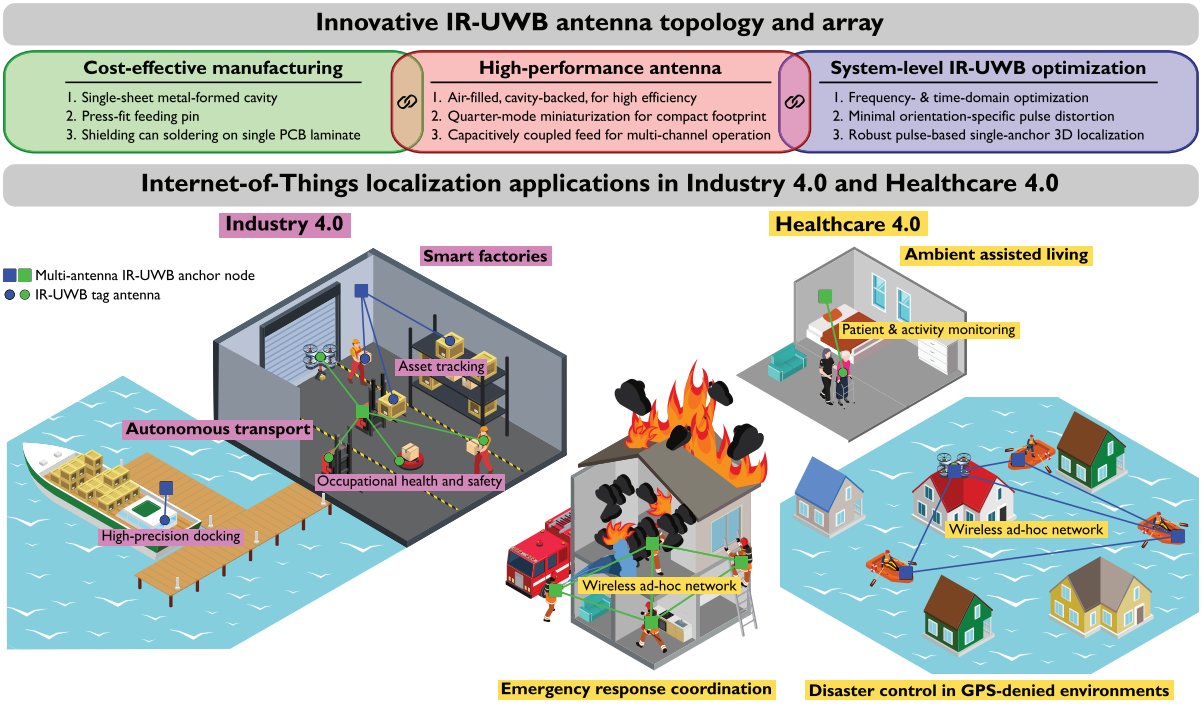

FIGURE 1. A novel cost-effective and high-performance air-filled cavity-backed IR-UWB antenna and antenna array are proposed. Their design leverages high-performance antenna design principles, compatibility with cost-effective manufacturing technologies and a rigorous system-level optimization process in the frequency and time domains. The proposed antenna array is a crucial building block for multi-channel, multi-antenna IR-UWB nodes for single-anchor 3D localization, which are adopted in a multitude of Internet-of-Things applications in Industry 4.0 and Healthcare 4.0 environments.

frequency and time domains has been analyzed and optimized for minimal orientation-specific pulse distortion [23], [25].

However, in [25], a clear trade-off between time-domain performance and achievable bandwidth was shown, limiting the number of supported UWB channels in a $\lambda_{min}/2 \times \lambda_{min}/2$ footprint (with λ_{min} the wavelength corresponding to the highest operating frequency of the antenna f_{max}). Moreover, these air-filled cavity-backed antennas are typically realized by Computer Numerical Control (CNC) milling [26], resulting in bulky and heavy antennas, or additive manufacturing [27], which requires additional metal components (tubelets). Other manufacturing techniques have been proposed for mmWave cavity-backed antennas, such as bulk silicon micro-electromechanical systems (MEMS) micromachining [28] or dedicated multilayer PCBs [29]. Yet, these technologies are expensive and require complex manufacturing processes [29], making them unsuitable for low-cost UWB antennas. More recently, the stacked-PCB air-filled substrate-integrated-waveguide (AFSIW) technology has enabled the use of low-cost PCB laminates [25], [30]. Yet, multiple PCB layers are required and the total material cost for a single antenna cavity [25] equals €2.5 (assuming a bulk order larger than 1000 cavities). Furthermore, the assembly process impedes inexpensive mass manufacturing, as perfect layer alignment and electrical contact between all layers are required [23].

In this manuscript, a cost-effective (less than €1) metal-stamped air-filled cavity-backed antenna element is presented for next-generation multi-channel, multi-antenna IR-UWB applications. The proposed antenna is conceived and designed by (1) adopting high-performance antenna design principles, (2) ensuring compatibility with low-cost manufacturing technologies and (3) performing a rigorous system-level optimization in the frequency and time domains (Fig. 1). It consists of a single RF PCB laminate, implementing a novel wideband grounded co-planar waveguide (GCPW)-to-probe feeding mechanism to enable multi-channel support (covering four UWB channels), and a single-sheet metal-formed cavity, which is deployed on the feed layer by standard pick-and-place techniques, providing a low-cost alternative for manufacturing air-filled cavities. An extensive sensitivity analysis proves that the antenna element is robust against manufacturing inaccuracies in the metal stamping process and that it achieves a high efficiency using low-cost materials. Furthermore, the antenna is optimized in both the frequency and time domains. In this optimization process, the metal stamping technology enables the realization of an arbitrary cavity height, offering an additional design parameter. Measurements demonstrate a fractional bandwidth (FBW) of 34.4 %, covering UWB channels (CHs) 5, 6, 8 and 9 of the IEEE 802.15.4-2024 standard [31], and a radiation efficiency η_{rad} of more than 91 %, in a compact $\lambda_{min}/2 \times_{min} /2$ footprint. The antenna also offers excellent time-domain performance, essential for pulse-based wireless systems [1], [3], [21], [25], as indicated by a measured relative group delay variation (GDV) of

only 68 ps and a measured system fidelity factor (SFF) of 99 %, along broadside. Exploiting the novel antenna element, a triple-antenna-array (TAA) is realized, exhibiting an isolation higher than 17.2 dB over the entire FBW and an isolation higher than 22.6 dB in the most prevalent UWB CH9. Therefore, it is excellently suited to serve as a multi-antenna anchor node for accurate and robust joint distance and 2D angle-of-arrival (AoA) estimation with a minimal number of antenna elements. AoA measurements, based on a low-complexity phase-difference-of-arrival (PDoA) algorithm, show accurate estimation results in stand-alone conditions, with mean absolute errors (MAEs) of 6.3 mm and 4.9° for the distance and angle estimates, respectively. Furthermore, robust estimation performance in realistic deployment conditions is highlighted through additional measurements with the TAA anchor deployed on a metal plate, with MAEs of 8.1 mm and 5.9° for distance and angle estimates, respectively, or a piece of drywall, with MAEs of 7.7 mm and 4.4° for distance and angle estimates, respectively. These results are obtained without recalibration with respect to the stand-alone measurements, enabling single-calibration single-anchor 3D localization in challenging Industry 4.0 and Healthcare 4.0 environments.

To the best of the author's knowledge, no metal-stamped IR-UWB cavity-backed antenna arrays are found in literature. The metal stamping technique is generally adopted to realize folded monopoles [32] or inverted-F antennas (IFAs) [33], [34]. However, these topologies offer limited gain and their radiation patterns exhibit significant variations in the angular and frequency domains. Moreover, they typically require ground plane clearance to maintain performance, unlike cavity-backed antennas, where the EM fields are confined to the antenna cavity. The same holds for commercially available metal-stamped antennas [35], [36], [37], which also prioritize compactness over performance. A metal-stamped antenna-in-package concept is presented in [38], simultaneously functioning as a heat sink for passive thermal management. Yet, the antenna is not optimized in the time-domain for IR-UWB applications. This is also the case for the slot antenna realized on a PCB shielding can in [39], which has an FBW of only 7 % and a total efficiency of only 71 % in simulations. Finally, in [40], a coupled-IFA antenna is proposed for IR-UWB localization. It is realized through CNC milling using brass sheets. Yet, its footprint is too large for incorporation in $\lambda/2$-spaced arrays. In Section III-C, the proposed metal-stamped air-filled cavity-backed antenna is thoroughly compared to the most relevant state-of-the-art metal-stamped antennas as well as to the stacked-PCB AFSIW cavity-backed IR-UWB antenna introduced in [25].

II. IR-UWB ARRAY: DESIGN AND MANUFACTURING

A. HARMONIZED ANTENNA TOPOLOGY AND MANUFACTURING PROCESS

A metal-stamped quarter-mode (QM) air-filled cavity-backed antenna element is conceived, specifically tailored towards multi-antenna IR-UWB applications in UWB channels 5, 6, 8 and 9 of the IEEE 802.15.4-2024 standard [31] (CH5: [6.24 GHz; 6.74 GHz], CH6: [6.74 GHz; 7.24 GHz], CH8: [7.24 GHz; 7.74 GHz] and CH9: [7.74 GHz; 8.24 GHz]). UWB CH5 and CH9, in particular, are the most widely supported UWB channels in academic and commercial applications, with CH9 expected to become the dominant channel in the future, as it is mandatory for high-band UWB operation [31]. Therefore, the design requirements listed in Table 1 are put forward. The proposed topology, depicted in Fig. 2, reconciles these stringent specifications with a compact 18.2 mm × 18.2 mm antenna footprint, corresponding to a $\lambda_{min}/2 \times \lambda_{min}/2$ footprint, with λ_{min} the wavelength at the highest operating frequency f_{max} = 8.24 GHz, and a straightforward manufacturing and assembly process.

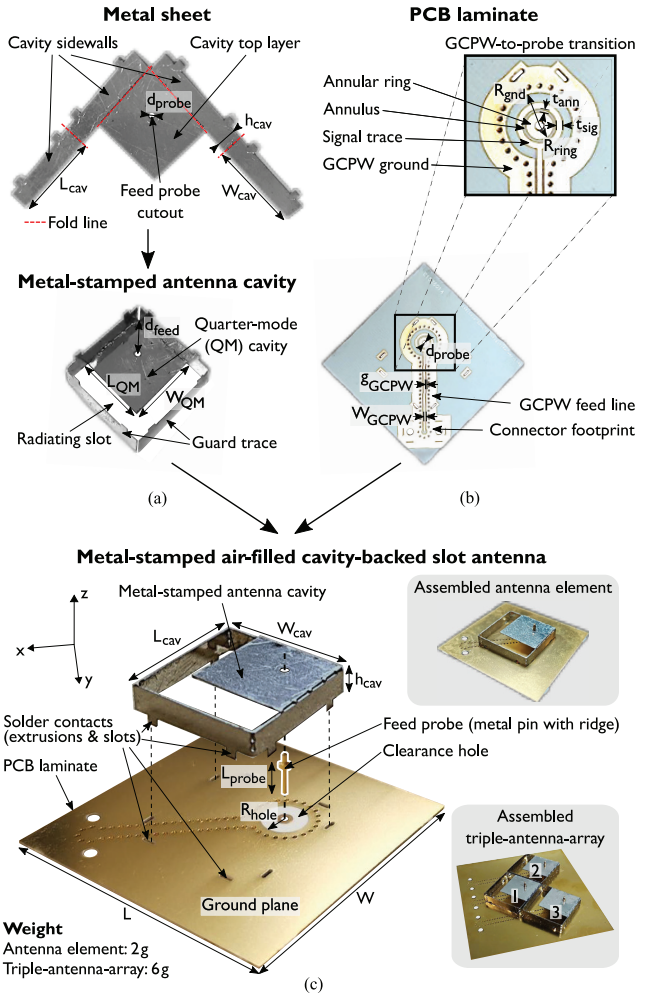

FIGURE 2. Antenna topology and assembly process: (a) metal-stamped antenna cavity, (b) feeding PCB containing GCPW-to-probe transition with capacitive coupling mechanism and (c) assembly process. Design parameters: $L = W = 35$ mm, $L_{cav} = W_{cav} = 17.5$ mm, $h_{cav} = L_{probe} = 3.4$ mm, $L_{QM} = W_{QM} = 12.8$ mm, $d_{feed} = 7.05$ mm, $d_{probe} = 1$ mm, $R_{ring} = 1.3$ mm, $t_{ann} = 0.45$ mm, $t_{sig} = 0.5$ mm, $R_{hole} = 2.8$ mm, $R_{gnd} = 3.35$ mm, $W_{GCPW} = 0.45$ mm and $g_{GCPW} = 0.25$ mm.

As indicated in Fig. 2a, the antenna cavity ($L_{cav} \times W_{cav} \times h_{cav}$) is realized by laser cutting a single 0.2 mm-

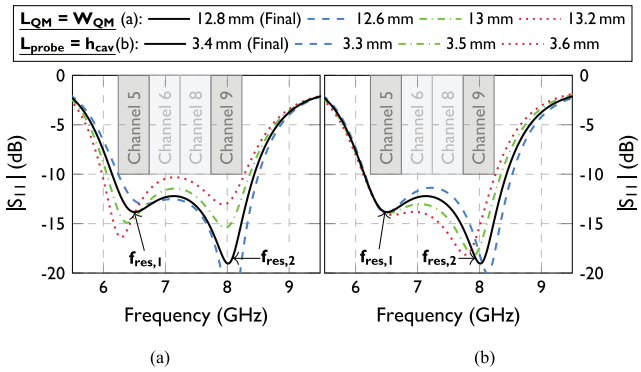

FIGURE 3. Parametric analysis of the metal-stamped antenna element. The $L_{QM} = W_{QM}$ and $L_{probe} = h_{cav}$ parameters are varied in (a) and (b), respectively, to show their effect on the resonance frequencies $f_{res,1}$ and $f_{res,2}$. The antenna covers UWB channels 5, 6, 8 and 9, as defined in the IEEE 802.15.4-2024 standard [31] (CH5: [6.24 GHz; 6.74 GHz], CH6: [6.74 GHz; 7.24 GHz], CH8: [7.24 GHz; 7.74 GHz] and CH9: [7.74 GHz; 8.24 GHz]).

TABLE 1. Design requirements, simulation and measurement results for the antenna element and triple-antenna-array (TAA). The worst-performing array element is listed for each figure-of-merit.

Quantity	Target	Antenna Element		TAA	
		CH5	CH9	CH5	CH9
FBW (%)	27.6	34.4 (31.6)		34.5 (31.9)	
Iso.* (dB)	> 15	-		> 17.2 (16.5)	> 22.6 (21.1)
η_{rad} (%)	> 85	> 98 (97)	> 91 (97)	> 93 (95)	> 90 (94)
GDV† (ps)	< 100	< 68 (90)	< 27 (60)	< 54 (93)	< 42 (75)
SFF† (%)	> 98	> 99 (99)	> 99 (99)	> 99 (99)	> 99 (99)

Table values: Measurements (Simulations), *Iso. = Isolation, †broadside

thick tinned steel sheet, after which an open cavity is formed by folding the cavity sidewalls. By attaching it to a single 0.254 mm-thick two-layer Rogers RO4350b high-frequency PCB laminate ($\epsilon_r = 3.66$ and $\tan\delta = 0.0037$), which implements the cavity's ground plane, a QM air-filled cavity-backed slot antenna is realized that resonates at frequency $f_{res,1}$. This resonance frequency is controlled by the QM cavity size $L_{QM} = W_{QM}$ (Fig. 2a), as shown by the $|S_{11}|$ parameter curves in Fig. 3a. The cavity's sidewalls constitute a guard trace (Fig. 2a) to increase shielding, essential for high isolation and compact array integration, and to define the borders of the antenna's radiating slot.

To excite the antenna element, a metal pin with a ridge (Fig. 2c) [41] is adopted to serve as feed probe (length L_{probe}, diameter d_{probe}). It is press-fit into the cavity's top layer to eliminate a solder contact. However, this also means that any feed enhancements, essential to obtain a sufficiently wideband antenna, need to be implemented in the PCB laminate constituting the antenna cavity's ground plane, in contrast to the antenna proposed in [25]. To this end, a 50 Ω GCPW feed, sharing the cavity's ground plane, and a novel GCPW-to-probe transition with incorporated capacitive coupling mechanism are proposed, as depicted in Fig. 2b.

The capacitive coupling, shown in detail in the inset in Fig. 2b, counteracts the inductance of the feed probe and introduces a second resonance at $f_{res,2}$. This resonance is controlled by the feed probe length L_{probe} (Fig. 2c, Fig. 3b), which directly determines the feed inductance, and the introduced capacitive coupling. The latter is realized by the annulus (width t_{ann}), separating the annular ring (radius R_{ring}) that is galvanically connected to the feed probe, and a concentric ring (width t_{sig}) interconnected to the GCPW signal trace, both on the backside of the PCB laminate. A clearance hole (radius R_{hole}) is implemented in the top metal layer of the PCB laminate (the cavity's ground plane, Fig. 2c), which allows further fine-tuning of the capacitive coupling. The proposed GCPW feed facilitates compact IC integration at the antenna backside, while the second resonance enlarges the impedance bandwidth, essential to enable multi-channel coverage.

The antenna is assembled by press-fitting the feed probe in the provisioned cutout in the metal-stamped cavity. Next, the cavity and feed probe are soldered to the PCB laminate. Note that the L_{probe} parameter is exactly equal to the h_{cav} parameter, since the feed probe is galvanically connected to the top of the cavity and to the feeding PCB, whose top plane also acts as the cavity's ground plane. The antenna's total material cost equals only €0.55, which represents a factor five cost reduction compared to stacked-PCB AFSIW antennas (assuming a production volume of 1000). The total cost includes the metal-stamped cavity (€0.5) and probe (€0.05) costs. The antenna is assumed to be deployed directly on a PCB (containing an IC) and reuses that PCB's ground plane. The assembly process is compatible with standard pick-and-place techniques, incurring negligible extra cost, in contrast to stacked-PCB AFSIW cavities. In the assembled prototype in this manuscript, the cavity is equipped with small extrusions that are inserted in slots in a dedicated PCB laminate, as indicated in Fig. 2c. The total weight of the antenna (cavity and PCB) is only 2 g.

B. DESIGN METHODOLOGY FOR IR-UWB OPTIMIZATION

The antenna's system-level time-domain characteristics are critical for applications that require accurate AoA estimation and 3D single-anchor UWB localization, such as the targeted use cases depicted in Fig. 1. A GDV below 100 ps and an SFF above 98 % are targeted (Table 1) over the antenna's entire positive hemisphere ($z > 0$) and for UWB channels 5, 6, 8 and 9, to minimize the orientation-specific pulse distortion and phase fluctuations introduced by the antenna. More specifically, within a UWB channel, the GDV is defined as the maximum deviation from the mean group delay introduced by an antenna link, whereas the SFF is defined as the cross-correlation between the channel-specific input and output pulses of that link [25]. To satisfy the imposed design requirements, a multi-domain optimization process [25] was carried out by exploiting the frequency-domain solver in CST Microwave Studio [42] and an in-house system-oriented simulation framework [21]. This framework enables the evaluation of the antenna's time-domain performance,

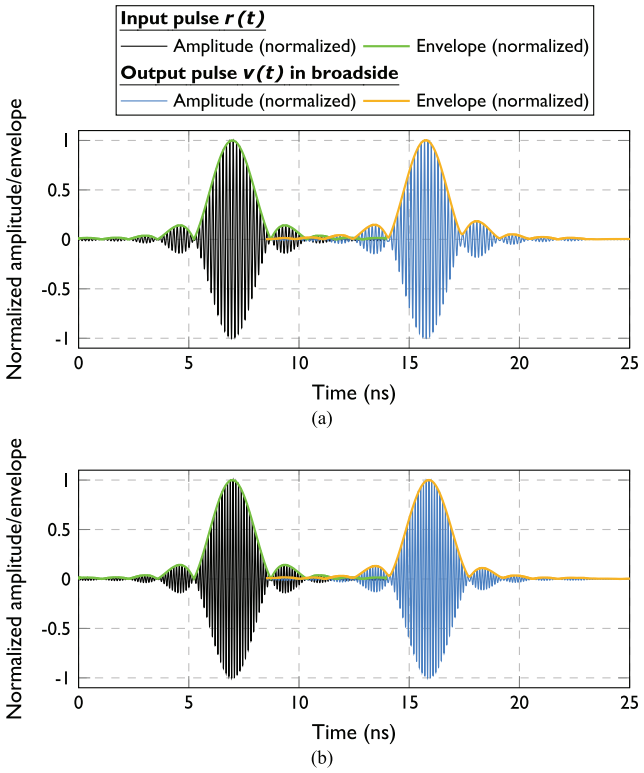

FIGURE 4. Time-domain antenna characterization: applied (reference) input pulses $r(t)$ and computed output pulses $v(t)$ in broadside, for an antenna link consisting of two prototypes of the proposed antenna element: (a) CH5 and (b) CH9.

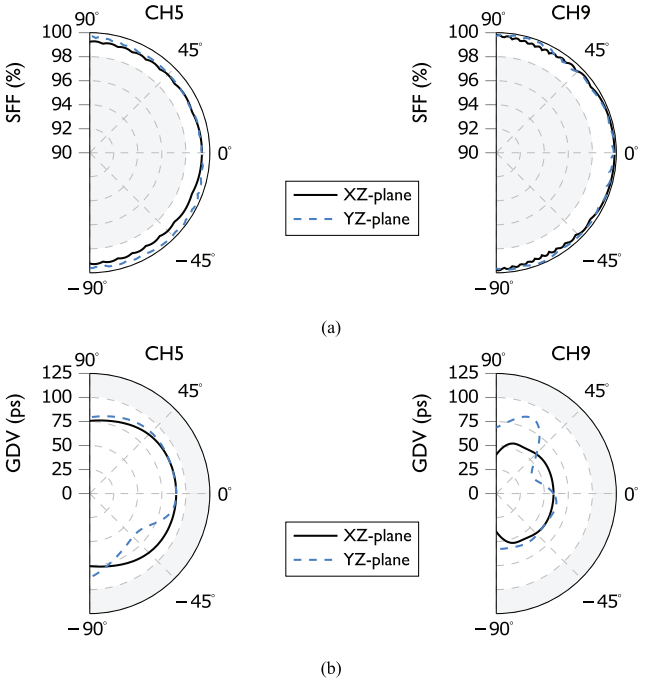

FIGURE 5. Time-domain simulation results of the antenna element in UWB CH5 and CH9: (a) system fidelity factor (SFF) and (b) relative group delay variation (GDV). The high SFF (> 98 %) and low GDV (< 100 ps) demonstrate the antenna's excellent pulse-preserving capabilities within its entire positive hemisphere (gray area), as required for robust and accurate pulse-based distance and angle-of-arrival (AoA) estimation.

by establishing a simulated antenna link, comprising two antenna elements and their over-the-air channel. To evaluate the system-level time-domain performance, the framework applies an input pulse $r(t)$ to this link and calculates the corresponding output pulse $v(t)$ to subsequently determine the GDV and SFF of the link. The IEEE 802.15.4-2024 standard [31] defines the appropriate reference input pulses $r(t)$ for each UWB channel. Fig. 4 depicts the normalized amplitude (black) and envelope (green) of these pulses for UWB CH5 and CH9.

In a first optimization step, the size of the antenna cavity $L_{\text{cav}} = W_{\text{cav}}$ and the QM cavity $L_{\text{QM}} = W_{\text{QM}}$ (Fig. 2a) were selected such that the antenna fits in an 18.2 mm × 18.2 mm footprint, and such that $f_{\text{res},1} = 6.49$ GHz, the center frequency of CH5 (Fig. 3a). An even smaller footprint could be obtained by reducing $L_{\text{cav}} = W_{\text{cav}}$ while keeping $f_{\text{res},1} = 6.49$ GHz, though at the cost of a narrower bandwidth. In a second step, the cavity height h_{cav} (Fig. 2a), which directly determines the feed probe length ($L_{\text{probe}} = h_{\text{cav}}$), and the capacitive coupling mechanism were exploited to optimize the antenna in the frequency domain. The capacitive coupling is predominantly determined by the R_{ring}, t_{ann}, t_{sig}, and R_{hole} parameters (Fig. 2b). These dimensions were tuned such that $f_{\text{res},2} = 7.99$ GHz, the center frequency of CH9 (Fig. 3b), to realize a large FBW covering four UWB channels, and such that the antenna radiation pattern variations in the frequency and spatial domain were minimized.

In the third step, the antenna's time-domain performance was optimized by starting from the frequency-domain-optimized design. The capacitive coupling mechanism (R_{ring}, t_{ann} and R_{hole}) was leveraged to tune the GDV and SFF. The R_{ring} and t_{ann} parameters were exploited to lower the GDV and to increase the SFF in both CH5 and CH9, by decreasing both dimensions. Decreasing R_{ring} also shifts $f_{\text{res},2}$ to higher frequencies, thereby increasing the antenna's FBW. However, these improvements are limited, as the antenna can no longer cover the entire target frequency band when the resonance frequencies $f_{\text{res},1}$ and $f_{\text{res},2}$ become too widely separated. Decreasing t_{ann} leads to the resonance frequencies shifting closer together, decreasing the FBW. This creates a clear trade-off between achieving a larger FBW and a lower GDV (and higher SFF). The R_{hole} dimension was specifically tuned to reduce the GDV in CH5, in order to meet the most stringent design requirement. Larger values lead to a reduced GDV and higher SFF in CH5, without significantly affecting the CH9 performance. However, variations in R_{hole} impact the antenna's FBW and shift its covered frequency band. Hence, the highest possible R_{hole}-value was selected to still retain the antenna's beneficial frequency-domain characteristics.

The cavity height h_{cav} was leveraged to improve the SFF in CH5 and CH9, without adversely affecting the GDV performance. Decreasing this dimension results in a higher SFF and larger FBW (Fig. 3b). Again, there is a limit to these improvements: when the resonance peaks are

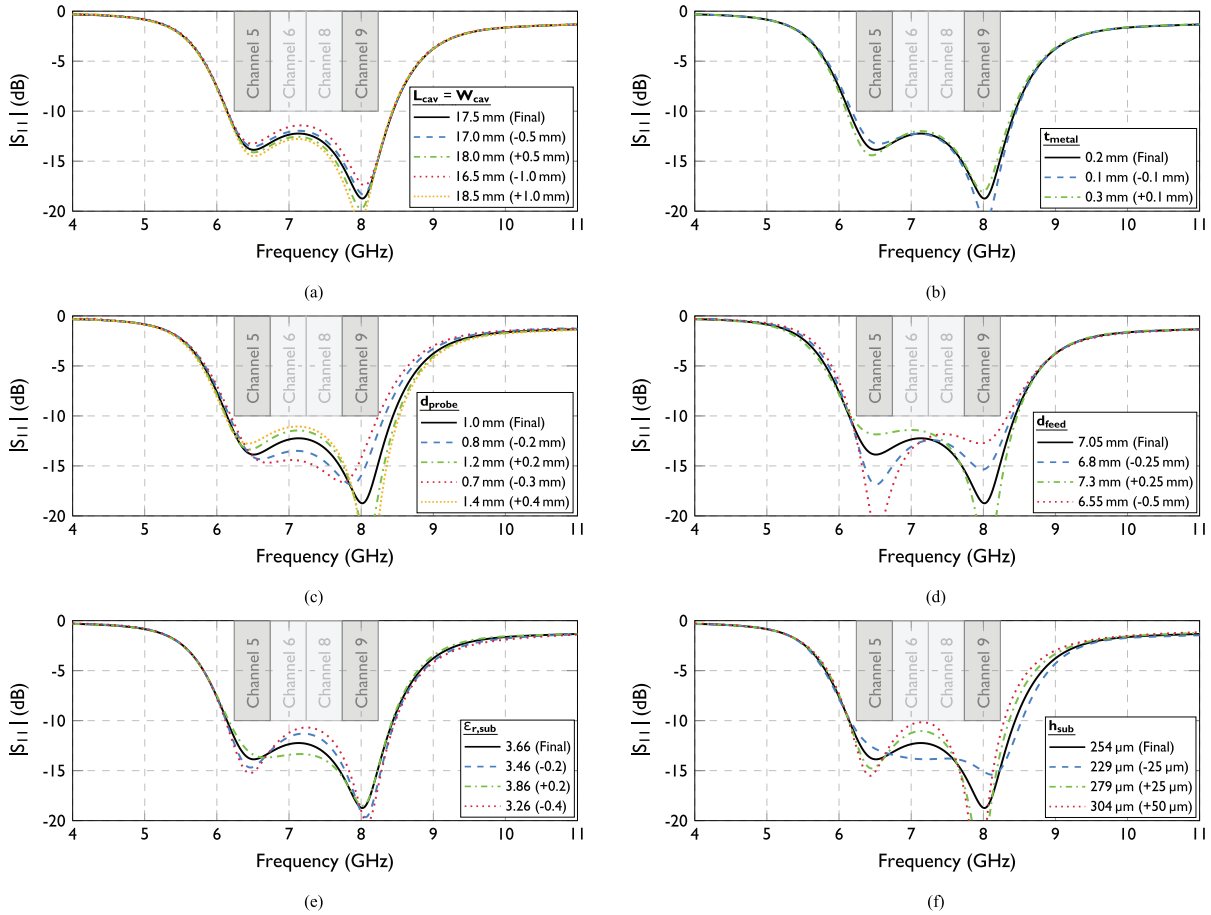

FIGURE 6. Sensitivity analysis of the metal-stamped antenna element: impact of design parameter variations on the antenna's reflection coefficient for the (a) $L_{cav} = W_{cav}$, (b) t_{metal}, (c) d_{probe}, (d) d_{feed}, (e) $\epsilon_{r,sub}$ and (f) h_{sub} parameters.

separated too far apart, the target frequency band is no longer fully covered. The antenna's metal stamping manufacturing process offers the advantage of realizing any arbitrary cavity height, allowing to precisely tune its SFF, such that the capacitive coupling mechanism can be exploited to focus on optimizing its GDV, leading to enhanced overall performance compared to conventional PCB-based AFSIW antennas [22], [23], [24], [25].

The final time-domain simulation results are depicted in Fig. 5. They prove that the imposed criteria are met in the XZ- and YZ-planes, and in CH5 and CH9. The high SFF (> 98 %) indicates that the antenna introduces minimal pulse distortion, as required for accurate and robust pulse-based IR-UWB positioning. The low GDV (< 100 ps) indicates that the antenna exhibits minimal phase variations over its wide frequency range, enabling accurate AoA estimation using low-complexity PDoA algorithms. The antenna's final design parameters are annotated in Fig. 2.

C. SENSITIVITY ANALYSIS: MANUFACTURING TOLERANCES AND MATERIAL PROPERTIES

To assess the effect of inaccuracies in its manufacturing and assembly process, the antenna was subjected to a thorough sensitivity analysis. More specifically, a series of simulations was carried out, introducing small variations in the antenna design parameters, exceeding typical manufacturing tolerances, to assess their impact on the antenna's reflection coefficient, radiation pattern and time-domain figures-of-merit. Focus was put on inaccuracies introduced by the metal stamping process (cutting and folding of a single metal sheet) and the feed probe, by analyzing variations in the $L_{QM} = W_{QM}$, $h_{cav} = L_{probe}$, $L_{cav} = W_{cav}$, d_{feed} and d_{probe} parameters, indicated in Fig. 2, and the metal sheet thickness t_{metal} (= 0.2 mm). The antenna feed substrate parameters, being the dielectric constant $\epsilon_{r,sub}$ and height h_{sub} (= 0.254 mm), were also considered.

The impact on the antenna's reflection coefficient $|S_{11}|$ of the $L_{QM} = W_{QM}$ and h_{cav} (= L_{probe}) parameters, which affect the resonance frequencies $f_{res,1}$ and $f_{res,2}$, respectively, is shown in Fig. 3. It is further discussed throughout Sections II-A and II-B. Fig. 6 shows the resulting reflection coefficients for variations in the other considered design parameters. Little impact is observed for variations in $L_{cav} = W_{cav}$ and t_{metal}. Changing d_{probe} slightly affects both resonances. When the feed probe becomes more narrow, the resonance peaks shift closer together, whereas a thicker probe causes the resonance peaks to separate further. The d_{feed} parameter determines how pronounced both resonances are,

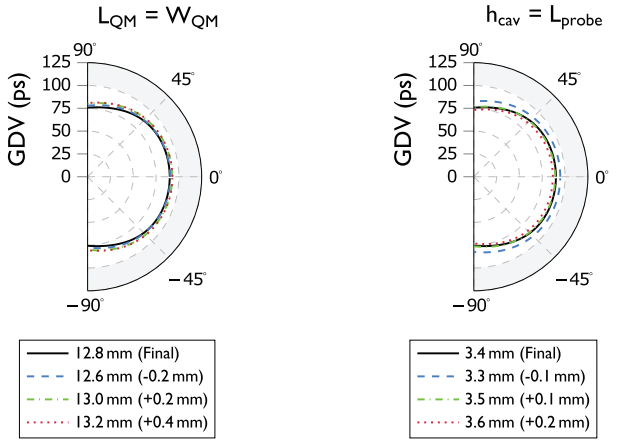

FIGURE 7. Sensitivity analysis of the metal-stamped antenna element: impact of design parameter variations on the antenna's GDV in CH5, in its XZ-plane, for the (a) $L_{QM} = W_{QM}$ and (b) $h_{cav} = L_{probe}$ dimensions.

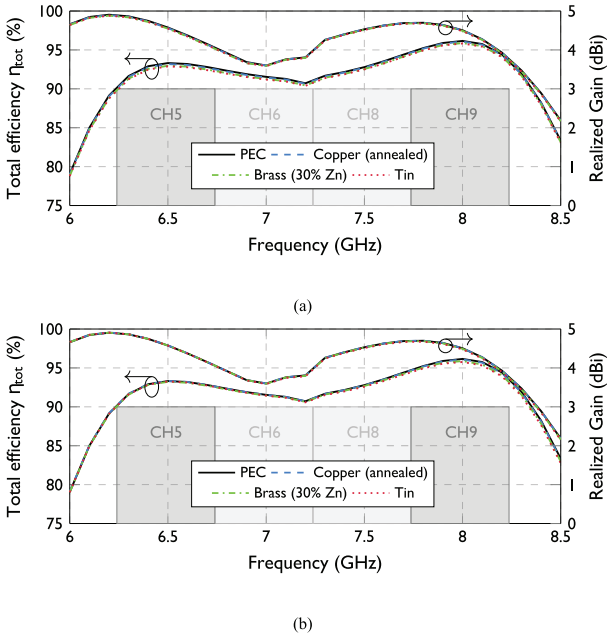

FIGURE 8. Effect of the adopted (a) metal-stamped cavity and (b) feed probe materials in the manufacturing process on the antenna's efficiency and realized gain: PEC ($\sigma = \infty$ S m^{-1}), annealed copper ($\sigma = 5.8 \cdot 10^7$ S m^{-1}), brass with 30% Zn ($\sigma = 1.67 \cdot 10^7$ S m^{-1}) and tin ($\sigma = 9.17 \cdot 10^6$ S m^{-1}).

with lower values leading to a more pronounced resonance peak at $f_{res,1}$ and higher values to a more pronounced resonance peak at $f_{res,2}$. Variations in $\epsilon_{r,sub}$ affect the coupling between both resonances, with higher values leading to increased coupling. Parameter h_{sub} also affects the coupling between both resonances and the resonance frequency $f_{res,2}$ itself, because it directly impacts the antenna's capacitively coupled feeding mechanism by fixing the distance between the annular ring and annulus on its substrate's backside (Fig. 2b), and the clearance hole on its top layer (Fig. 2c).

The sensitivity analysis demonstrates that the antenna still covers the necessary bandwidth for substrate parameter variations significantly exceeding the typical manufacturing tolerances of the adopted Rogers RO4350b material ($\epsilon_{r,sub} \pm 0.05$, $h_{sub} \pm 25\,\mu$m), and for deviations up to at least 0.2 mm in any of the cavity and feed probe design parameters, which is twice the typical tolerance for sheet metal laser cutting ($\pm$ 0.1 mm). Furthermore, it was found that similar variations in any of the aforementioned design parameters result in negligible impact on the antenna's radiation pattern and time-domain figures-of-merit (GDV and SFF), for any UWB channel. Fig. 7 illustrates this for the GDV in CH5 in the antenna's XZ-plane, considering variations in the $L_{QM} = W_{QM}$ and $h_{cav} = L_{probe}$ parameters. Clearly, the GDV remains nearly unaffected, making the antenna very robust against manufacturing inaccuracies in the metal stamping process.

During the antenna assembly process (Fig. 2c), the cavity extrusions and slots in its PCB ground plane enable accurate alignment between the metal-stamped cavity and the ground plane. The feed probe is aligned by means of cutouts in the cavity and PCB. Its ridge further facilitates alignment and galvanic contact with the cavity. Nevertheless, the impact of potential misalignment between cavity, ground plane and feed probe was also analyzed through simulations. It was found that the antenna retained its characteristics for cavity and feed probe displacements up to 0.5 mm and for rotational mismatches up to 30°. Hence, misalignment yields negligible influence on the antenna characteristics, compared to the effect of design parameter variations, discussed previously.

Finally, the impact on the antenna performance of the selected materials in the manufacturing process was also analyzed. The antenna is realized from a 0.2 mm-thick (t_{metal}) tinned steel sheet consisting of a 0.2 mm-thick core layer of low-carbon steel (a ferromagnetic material with an electrical conductivity $\sigma = 6.6 \cdot 10^6$ S m^{-1} and a relative magnetic permeability $\mu_r \approx 2000$) and an approximately 2 µm-thick coating made of tin ($\sigma = 9.17 \cdot 10^6$ S m^{-1}, $\mu_r \approx 1$). Calculating the skin depth of both materials at the lowest frequency of operation $f_{min} = 6.24$ GHz yields 2.1 µm for the tin coating and 55 nm for the core steel layer, respectively. Hence, the current in the tinned steel sheet mainly flows through the non-magnetic (diamagnetic) tin coating and magnetic losses are minimized. The feed probe is a tin-plated brass pin with a diameter of 1 mm (d_{probe}) [41]. Because tin and brass are both non-magnetic materials ($\mu_r \approx 1$), magnetic losses in the feed probe can also be neglected.

To determine the effect of the electrical conductivity σ of the metal-stamped cavity and feed probe materials on the antenna performance, simulations were conducted, focusing on the antenna's FBW, total efficiency η_{tot} and realized peak gain. Several σ-values were considered, corresponding to the adopted antenna materials: copper (equivalent to brass with 0 % Zn), brass (with 30 % Zn) and tin. The performance of a fictitious antenna, with a cavity and feed probe made of perfect electrically conducting (PEC) material, served as a benchmark. The skin effect was also included in the simulations. Fig. 8 shows the simulation

results of the antenna's total efficiency and realized peak gain. Clearly, there is little to no difference between the considered materials. The same holds for the FBW, which is not explicitly shown.

Compared to the benchmark antenna, the selected materials do not impact antenna performance, in terms of their electrical conductivity and magnetic properties. Material thickness variations do not affect antenna performance either (as indicated by the sensitivity analysis on t_{metal} and d_{probe}). Hence, by making a suitable material choice (tinned steel cavity and tin-plated brass feed probe), a high-performance antenna was conceived, while adopting low-cost and manufacturing-friendly materials.

D. TRIPLE-ANTENNA-ARRAY FOR JOINT DISTANCE AND 2D AOA ESTIMATION

The proposed antenna element is exploited to realize a V-shaped TAA, as depicted in Fig. 2c. A three-element array was adopted because this is the minimum number of elements required to estimate the AoA in both azimuth and elevation planes. This is needed for single-anchor 2D AoA estimation and, consequently, 3D IR-UWB positioning. Moreover, this choice prioritizes minimal cost and size, crucial factors for the targeted IR-UWB applications depicted in Fig. 1. The TAA is arranged in a V-shape to maintain symmetry in the azimuth plane. This improves the inter-element isolation and AoA estimation accuracy, compared to a triangle-shaped TAA (with two bottom elements and a third element that is centered on top), as verified in simulations. The inter-element distance is fixed to 18.2 mm.

Because of its high self-shielding, the proposed antenna element can be directly incorporated in this array configuration without reoptimization, yielding high performance, as shown in Table 1. Moreover, it can be incorporated in larger arrays, which can offer improved positioning accuracy, albeit with an increase in cost (manufacturing cost and increased number of transceivers) and size, and with increasingly more marginal improvements in accuracy as the number of elements grows [10]. Simulations of a 2 × 2 and 3 × 3 array confirm the antenna element's robust performance in these larger arrays without reoptimization, exhibiting a worst-case (over all array elements) FBW of 30.2 % and a worst-case efficiency exceeding 94 %. The inter-element isolation is similar compared to the V-shaped TAA, with a worst-case isolation of 14.2 dB in CH5 and 17.5 dB in CH9.

The TAA is realized by soldering three metal-stamped cavities with press-fit feed probes to a single PCB laminate, resulting in a total cost of only € 1.65 and a total weight of only 6 g (cavities and PCB), excluding connectors.

III. ANTENNA PERFORMANCE: NUMERICAL RESULTS AND EXPERIMENTAL VALIDATION

A. ANTENNA ELEMENT AND TRIPLE-ANTENNA-ARRAY

The frequency- and time-domain performance of the antenna element and the TAA were verified in an anechoic chamber,

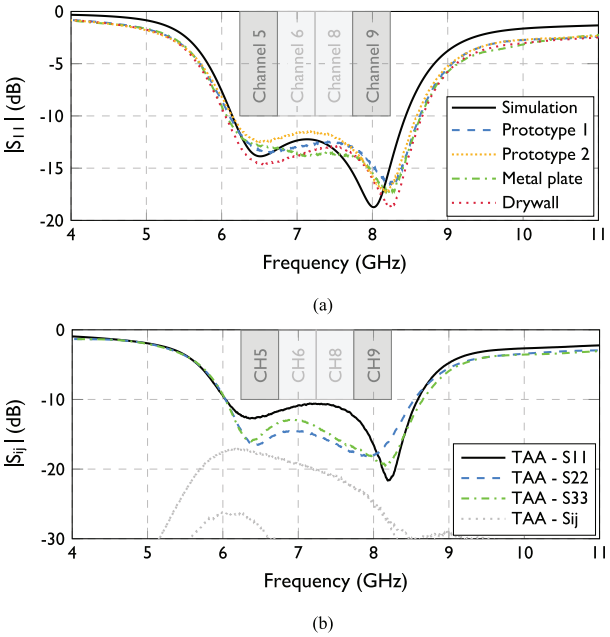

FIGURE 9. (a) Measured and simulated reflection coefficient of the antenna element (two prototypes) in different deployment scenarios and (b) measured *S*-parameters (reflection coefficients and mutual coupling) of the TAA in free-space stand-alone conditions.

using a Keysight N5242b PNA-X network analyzer and an NSI-MI spherical near-field scanner system. For ease of measurements, the prototypes are equipped with a GCPW connector footprint (Fig. 2b) for Southwest's 2.92 mm vertical-launch connectors [43] and the GCPW feed lines of the TAA are routed along its PCB backside to realize three in-line connector feeds (Fig. 2c). A summary of the measurement results is presented in Table 1.

The reflection coefficient and the radiation patterns of the single antenna element were measured in free-space stand-alone conditions and when deployed on a 30 cm × 30 cm metal plate and a 30 cm × 30 cm piece of drywall. The measured reflection coefficients are shown in Fig. 9a, together with the free-space simulation result. A good agreement is obtained for two different prototypes, achieving an FBW of 34.4 % and covering the targeted frequency band. A slight deviation of $f_{\text{res},2}$ is noticeable, caused by manufacturing inaccuracies of the cavity height h_{cav} (Fig. 3b). Yet, the antenna element remains matched when directly deployed on the metal plate and drywall, indicating robust performance in actual deployment conditions. The antenna element's measured radiation patterns are shown in Fig. 10, together with the free-space simulation result. Again, the measurements agree well with simulations and limited radiation pattern deformation is observed when the antenna element is deployed on the drywall. Slightly larger gain fluctuations are observed when it is deployed on the metal plate, caused by diffraction along the plate's edges. Note that the radiation patterns are shown at the center frequencies of CH5 and CH9, which are the outer channels of the considered

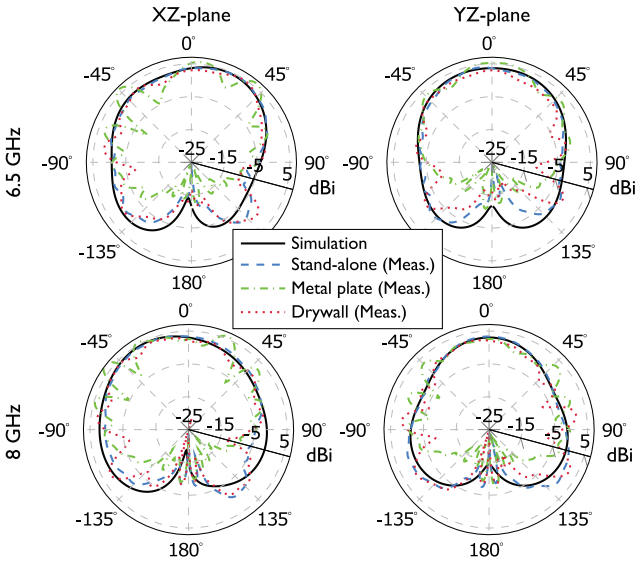

FIGURE 10. Measured and simulated radiation patterns of the antenna element at 6.5 GHz and 8 GHz, respectively, in different deployment scenarios. Limited radiation pattern deformation demonstrates robust antenna performance in challenging real-life environments.

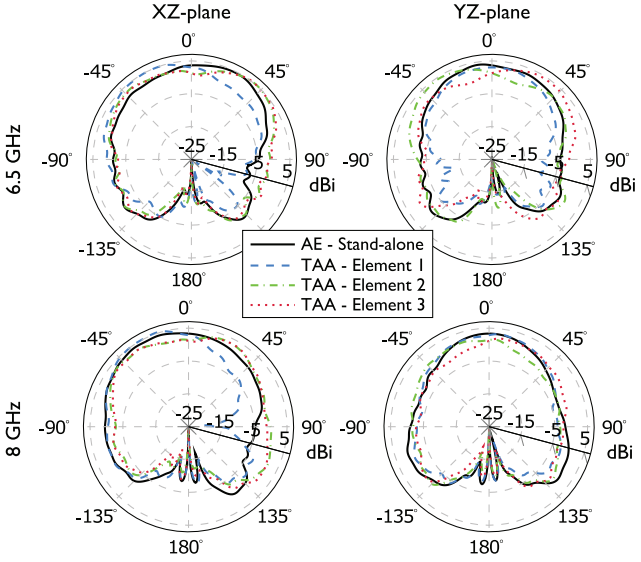

FIGURE 11. Measured radiation patterns of the stand-alone antenna element (AE) and the embedded antenna elements in the triple-antenna-array (TAA), at 6.5 GHz and 8 GHz, respectively. The radiation patterns of the TAA elements are very similar to each other and to the AE radiation pattern, indicating that the AE retains its performance after incorporation in the TAA.

UWB frequency band. Similar results were obtained for CH6 and CH8.

System-level time-domain measurements were conducted by setting up an antenna link between two single-element prototypes in an anechoic chamber and by measuring the S-parameters of this link to determine its transfer function. Impact from the measurement setup was minimized by using high-performance and phase-stable cables connecting the antenna elements to the network analyzer. Moreover, to accurately measure the over-the-air antenna link, a calibration was performed to ensure that the port planes were situated at the antenna connectors. Measurement-induced pulse distortion was minimized by measuring the transfer function over a wide frequency range from DC to 26.5 GHz. To determine the GDV and SFF, the same channel-specific reference input pulses $r(t)$ as in the simulations, were applied to the antenna link (Fig. 4). Based on the measured transfer function, the corresponding output pulses $v(t)$, the GDV and the SFF were computed, using an in-house framework [21]. Fig. 4 also depicts the normalized amplitude (blue) and envelope (yellow) of the output pulses $v(t)$ for CH5 and CH9, in broadside direction. Clearly, there is no visually apparent pulse distortion, translating to an SFF higher than 99 % and a GDV below 68 ps. The obtained measurement results prove slightly better than predicted by simulations, as also seen in the summary of the measured and simulated antenna specifications, given in Table 1.

The TAA was also characterized in the frequency and time domains, similar to the antenna element. Fig. 9b depicts the measured S-parameters of the TAA, yielding an FBW of at least 34.5 %, with an isolation of at least 17.2 dB over the entire FBW and an isolation of at least 22.6 dB over all of CH9. Fig. 11 shows the embedded radiation patterns of the TAA elements, indicating limited deformation with respect to the antenna element's stand-alone radiation pattern. During all measurements, the TAA ports were terminated by 50 Ω loads. The radiation patterns are again shown at the center frequencies of CH5 and CH9, and again similar results were obtained for CH6 and CH8. To determine the time-domain figures-of-merit, the antenna link now consisted of a TAA and an antenna element prototype. Table 1 shows that all measurements correspond well with simulations, that all target specifications are met, and that the antenna element retains its performance after incorporation in the TAA, without reoptimization.

B. SINGLE-ANCHOR DISTANCE AND 2D AOA ESTIMATION

Joint distance and 2D AoA measurements were conducted using a TAA prototype, demonstrating its potential for single-anchor 3D IR-UWB positioning. Therefore, the TAA and a single antenna element, acting as the tag antenna, were mounted on an NSI-MI spherical scanner system in an anechoic chamber, as shown in Fig. 12. By rotating the anchor around its x and z axes via the Φ_{NSI} and Θ_{NSI} rotational axes of the NSI-MI system, as shown in Fig. 12a, and thereby changing the AoA coordinate system (green), while keeping the tag fixed, the situation is mimicked where the tag is rotating around the anchor at a fixed distance d = 2.55 m and with varying AoAs (azimuth AoA ϕ, elevation AoA θ) from the perspective of the anchor, as shown in Fig. 12b. Note that this coordinate system is different from the one defined in Fig. 2 of the manuscript.

Cable displacement during anchor rotation was minimized by employing a rotational joint in combination with a three-to-one RF switch [44], which was directly connected to

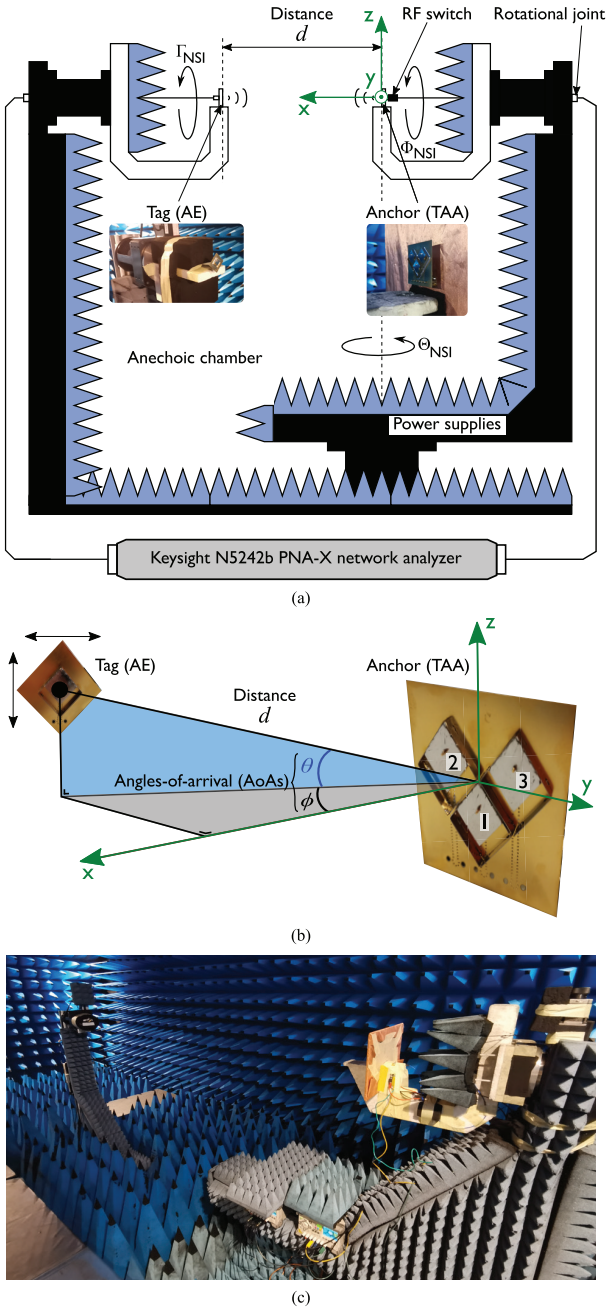

FIGURE 12. Dedicated measurement setup for joint distance (d) and 2D AoA (ϕ, θ) estimation validation: (a) schematic overview, (b) AoA definitions and (c) picture.

the three in-line feeds of the TAA (Fig. 12 and Fig. 2c). Furthermore, for any given tag-anchor position, the tag was rotated around its own axis (the Γ_{NSI} rotational axis of the NSI-MI system, Fig. 12a) to minimize polarization mismatch. The measurement setup was fully automated, using programmable power supplies to configure the RF switch, and care was taken to perform separate calibration steps for every state of the RF switch, which were automatically reloaded every time a different anchor element was selected, to ensure that the port planes were situated at the connectors of the TAA and the antenna element. A picture of the measurement setup is included in Fig. 12c.

Measurements were conducted for the more prevalent CH5 and CH9 [31], and when the anchor was deployed in free space, on a 30 cm × 30 cm metal plate and on a 30 cm × 30 cm piece of drywall. Distance (d) and AoA (ϕ, θ) estimates were obtained through S-parameter measurements between the tag and the three antenna elements in the anchor TAA, using a Keysight N5242b PNA-X network analyzer, as in [25]. The distance estimates were derived by averaging the time-of-arrival-based estimates for each anchor element. The AoA estimates were computed from the 1D AoAs for each pair of anchor elements, which were obtained from the S-parameter phase differences between the elements in each pair, using a low-complexity PDoA algorithm [12]. A one-time calibration step was conducted by applying a dissimilarity factor [45] and a compensation for measurement setup misalignment [25]. This calibration step was performed once and in free-space stand-alone conditions only. The resulting calibration coefficients were applied for all estimation experiments (free space, metal plate and drywall). Note that similar experiments could be conducted by interconnecting the anchor TAA and tag antenna element to a UWB transceiver platform [11], [12]. Yet, the objective in this manuscript is to isolate and examine the specific effects of the antenna array, independent of the transceiver's influence.

Fig. 13 shows the 2D AoA estimation results, as a function of the real AoAs (black solid line), for the azimuth ϕ and elevation θ angles, for the three different integration scenarios (free space, metal plate and drywall), and for CH5 (Fig. 13a) and CH9 (Fig. 13b). A field-of-view of [-60°, 60°] × [-60°, 60°] is considered, and both uncalibrated (blue) and calibrated (green) AoA estimates are depicted. It is observed that the uncalibrated AoA estimates are already accurate, highlighting the excellent antenna characteristics. Moreover, they are very similar over the three integration scenarios. Hence, applying the calibration improves the AoA estimation accuracy for all three integration scenarios, even with the system only being calibrated (once) in free-space stand-alone conditions. Fig. 13 shows that this holds for both azimuth and elevation angle estimations, and for CH5 and CH9, proving accurate and robust 2D AoA estimation over multiple UWB channels.

The cumulative distribution functions (CDFs) of the distance, azimuth AoA and elevation AoA estimation errors, are depicted in Fig. 14, after calibration, and for CH5 (top) and CH9 (bottom). In free-space conditions, an MAE and standard deviation σ_{d} of 6.3 mm and 8.0 mm, respectively, are obtained for the distance estimation errors. An MAE and standard deviation σ_{AoA} of 4.9° and 7.2°, respectively, are obtained for the angle estimation errors. In other words, 98 % of distance estimates differ less than 2 cm from the ground truth and 92 % of AoA estimates are accurate within 10°, showcasing accurate joint distance and 2D AoA estimation with only three antenna elements. The estimation errors are approximately the same in CH5 and CH9. Furthermore, the

TABLE 2. Comparison with state-of-the-art metal-stamped and AFSIW cavity-backed IR-UWB antenna elements.

Ref.	f_0 (GHz)	Manufacturing technology	Footprint ($\lambda_0 \times \lambda_0$)	FBW (%)	UWB channels	η_{tot} (%)	Time-domain SFF (%)	Time-domain GDV (ps)	Cost† (€)	Array
[25]	6.49	Stacked-PCB AFSIW	0.41×0.41	17.6	CH5, CH7	> 91	> 98.8	< 93	2.5	2D (square 2×2)
[34]	2.44	Metal-stamping	0.20×0.12	22.2	-	< 60	-	-	-	-
[38]	28.5	Metal-stamping	0.33×0.29	2.4	-	-	-	-	-	1D (linear 1×8)
[39]	7.99	Metal-stamping	0.53×0.39	7.0*	CH9	> 71*	-	-	-	-
[40]	3.99	CNC-milling	1.20×0.65	37.5	CH1, CH2, CH3, CH4	> 85	> 90	-	-	-
This	**7.37**	**Metal-stamping**	**0.43×0.43**	**34.4**	**CH5, CH6, CH8, CH9**	**> 90**	**> 99**	**< 68**	**0.55**	**2D (V-shaped TAA)**

*Simulation result †Single-antenna element

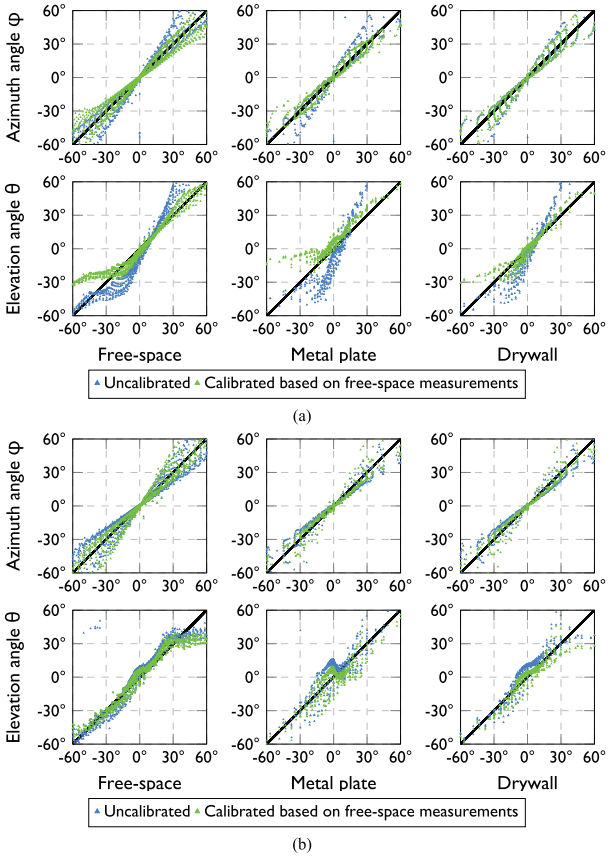

FIGURE 13. Calibrated and uncalibrated 2D AoA estimation results when the anchor was deployed in free space, on a metal plate and on a piece of drywall, for (a) CH5 and (b) CH9.

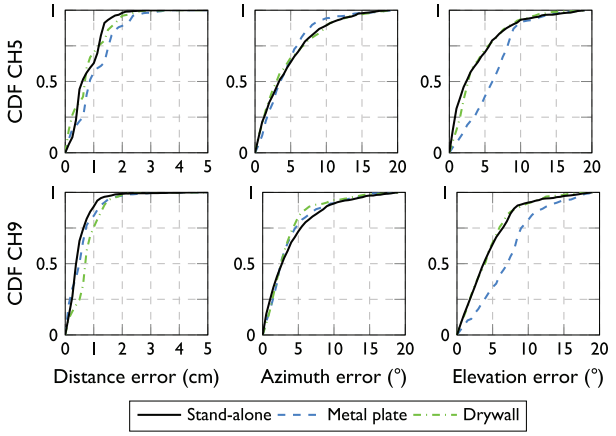

FIGURE 14. Cumulative distribution functions (CDFs) of distance, azimuth angle and elevation angle estimation errors, for CH5 and CH9, when the anchor was deployed in free space, on a metal plate and on drywall.

estimation errors are similar when the anchor is mounted on a metal plate (94 % of distance estimates accurate within 2 cm and 90 % of AoA estimates within 10°, MAEs of 8.1 mm and 5.9°, respectively, and σ_d of 10.4 mm and σ_{AoA} of 7.9°) or a piece of drywall (98 % of distance estimates accurate within 2 cm and 92 % of AoA estimates within 10°, MAEs of 7.7 mm and 4.4°, respectively, and σ_d of 8.6 mm and σ_{AoA} of 6.3°). Hence, accurate estimation is achieved in these conditions as well, with the system being calibrated in free-space stand-alone conditions only, highlighting the robustness of the proposed TAA anchor in Industry 4.0 and Healthcare 4.0 applications, as well as its excellent one-time-calibration performance. Considering the combined estimates in all deployment conditions, yields an overall MAE of 7.1 mm and σ_d of 8.9 mm for all distance estimation errors, with 97 % of distance estimates differing less than 2 cm from the ground truth. For the angle estimation errors, a combined MAE of 5.0° and σ_{AoA} of 7.2° are obtained, with 91 % of AoA estimates accurate within 10°.

C. COMPARISON WITH STATE-OF-THE-ART

Table 2 compares the proposed antenna to the state-of-the-art metal-stamped and AFSIW cavity-backed UWB antenna elements discussed in Section I. Clearly, the proposed antenna offers the largest FBW in a $\lambda_{min}/2 \times \lambda_{min}/2$ footprint. Although the design in [40] offers a slightly larger FBW, its footprint is more than twice as large. The proposed antenna's novel feeding mechanism and QM-miniaturization technique, reducing an air-filled cavity's footprint by a factor four, enable the realization of a compact antenna element that covers four UWB channels. Moreover, owing to its rigorous system-level and time-domain optimization process, it significantly outperforms the other metal-stamped antenna elements in terms of efficiency and time-domain performance. Compared to the stacked-PCB AFSIW cavity-backed antenna, the proposed metal-stamped antenna element offers

a significant decrease in manufacturing complexity, yielding a factor five cost reduction. Furthermore, it enables arbitrary cavity heights, leading to better time-domain performance (higher SFF, lower GDV), over a larger frequency range, as evidenced by Table 2. This results in nearly identical localization accuracy to [25], with one fewer array element.

IV. CONCLUSION

A compact ($0.43\,\lambda_0 \times 0.43\,\lambda_0$), lightweight (2 g) and high-performance ($\eta_{\text{tot}} > 90\,\%$) metal-stamped QM air-filled cavity-backed slot antenna was proposed. The topology, consisting of only a single PCB laminate, a metal feeding pin, and a single sheet of metal, facilitates compatibility with cost-effective metal stamping manufacturing techniques, resulting in a total manufacturing cost of only €0.55. A novel capacitively coupled wideband feeding mechanism, incorporated in a single-PCB GCPW-to-probe transition, has been conceived to counteract the feed probe's inductance and to introduce a second resonance, significantly increasing the operational bandwidth (FBW = 34.4 %) and enabling multi-channel support, covering UWB channels 5, 6, 8 and 9. Joint optimization of the antenna element in the frequency and time domains yields a GDV of 68 ps and an SFF of 99 %, demonstrating that the antenna introduces minimal phase variations and minimal pulse distortion, enabling accurate and robust pulse-based AoA estimation using low-complexity PDoA algorithms, making the antenna excellently suited for IR-UWB positioning applications. A comparison with other state-of-the-art metal-stamped and IR-UWB AFSIW cavity-backed antenna elements indicates that the proposed solution is capable of providing high radiation efficiency ($\eta_{\text{rad}} > 91\,\%$) and excellent time-domain performance over a wide bandwidth, while maintaining a compact footprint and thin profile, and this without requiring expensive multi-layered high-frequency laminates or complex time-consuming assembly techniques. Furthermore, an extensive sensitivity analysis proved that the antenna is robust against manufacturing inaccuracies in the metal stamping process. The antenna element was exploited to realize a V-shaped TAA exhibiting a high isolation over a wide bandwidth, outperforming the designs in [12] and [25], specifically for low-complexity joint distance and 2D AoA estimation. Excellent estimation accuracy was obtained in free-space conditions and when the TAA was mounted on a metal plate or a piece of drywall, while being calibrated based on free-space measurements. This highlights the high antenna-to-integration-platform isolation of the proposed solution, marking an important step towards single-anchor 3D localization in challenging Industry 4.0 and Healthcare 4.0 environments.

REFERENCES

[1] M. Elsanhoury, P. Mäkelä, J. Koljonen, P. Välisuo, A. Shamsuzzoha, T. Mantere, M. Elmusrati, and H. Kuusniemi, "Precision positioning for smart logistics using ultra-wideband technology-based indoor navigation: A review," *IEEE Access*, vol. 10, pp. 44413–44445, 2022.

[2] U.-S. Suh, G. Lee, J. Han, T. W. Kim, and W.-S. Ra, "Passive IR-UWB localization system for UAV-based electric facility inspection during GPS outage," *IEEE Access*, vol. 11, pp. 39597–39608, 2023.

[3] A. Benouakta, F. Ferrero, L. Lizzi, and R. Staraj, "Advancements in industrial RTLSs: A technical review of UWB localization devices emphasizing antennas for enhanced accuracy and range," *Electronics*, vol. 13, no. 4, p. 751, Feb. 2024.

[4] K. Guo, X. Li, and L. Xie, "Ultra-wideband and odometry-based cooperative relative localization with application to multi-UAV formation control," *IEEE Trans. Cybern.*, vol. 50, no. 6, pp. 2590–2603, Jun. 2020.

[5] L. Lou, Q. Li, Z. Zhang, R. Yang, and W. He, "An IoT-driven vehicle detection method based on multisource data fusion technology for smart parking management system," *IEEE Internet Things J.*, vol. 7, no. 11, pp. 11020–11029, Nov. 2020.

[6] H. H. Helgesen, T. Fuglestad, K. Cisek, B. Vik, Ø. K. Kjerstad, and T. A. Johansen, "Inertial navigation aided by ultra-wideband ranging for ship docking and harbor maneuvering," *IEEE J. Ocean. Eng.*, vol. 48, no. 1, pp. 27–42, Jan. 2023.

[7] L. Barbieri, M. Brambilla, A. Trabattoni, S. Mervic, and M. Nicoli, "UWB localization in a smart factory: Augmentation methods and experimental assessment," *IEEE Trans. Instrum. Meas.*, vol. 70, pp. 1–18, 2021.

[8] Y. Zhang and L. Duan, "A phase-difference-of-arrival assisted ultra-wideband positioning method for elderly care," *Measurement*, vol. 170, Jan. 2021, Art. no. 108689.

[9] J. Tiemann, O. Fuhr, and C. Wietfeld, "CELIDON: Supporting first responders through 3D AOA-based UWB ad-hoc localization," in *Proc. 16th Int. Conf. Wireless Mobile Comput., Netw. Commun. (WiMob)*, Oct. 2020, pp. 20–25.

[10] Y.-Y. Li, G.-Q. Qi, and A.-D. Sheng, "Performance metric on the best achievable accuracy for hybrid TOA/AOA target localization," *IEEE Commun. Lett.*, vol. 22, no. 7, pp. 1474–1477, Jul. 2018.

[11] M. Zhao, T. Chang, A. Arun, R. Ayyalasomayajula, C. Zhang, and D. Bharadia, "ULoc: Low-power, scalable and cm-accurate UWB-tag localization and tracking for indoor applications," *Proc. ACM Interact., Mobile, Wearable Ubiquitous Technol.*, vol. 5, no. 3, pp. 1–31, Sep. 2021.

[12] T. Margiani, S. Cortesi, M. Keller, C. Vogt, T. Polonelli, and M. Magno, "Angle of arrival and centimeter distance estimation on a smart UWB sensor node," *IEEE Trans. Instrum. Meas.*, vol. 72, pp. 1–10, 2023.

[13] J. K. Rai, P. Ranjan, R. Chowdhury, and M. Jamaluddin, "Quad port MIMO Al_2O_3 ceramic based integrated reconfigurable wideband sensing and communication dielectric antenna for 5G cognitive radio," *IEEE Trans. Compon., Packag., Manuf. Technol.*, vol. 15, no. 1, pp. 94–103, Jan. 2024.

[14] Z. Lasemiimeni, Z. Atlasbaf, and N. Karbaschi, "Dual-functional ultrawideband antenna with high fidelity factor for body area networks and microwave imaging systems," *IEEE Access*, vol. 9, pp. 112930–112941, 2021.

[15] (2018). *DW1000 Hardware Design Guide*. Accessed: Dec. 21, 2024. [Online]. Available: https://www.qorvo.com/products/p/DW1000#documents

[16] R. Chandel, A. K. Gautam, and K. Rambabu, "Design and packaging of an eye-shaped multiple-input–multiple-output antenna with high isolation for wireless UWB applications," *IEEE Trans. Compon., Packag., Manuf. Technol.*, vol. 8, no. 4, pp. 635–642, Apr. 2018.

[17] M. Kaushik, J. K. Dhanoa, and M. K. Khandelwal, "Partially omnidirectional and circularly polarized MIMO antenna covering sub-6-GHz band for 5G fast plan," *IEEE Trans. Compon., Packag., Manuf. Technol.*, vol. 13, no. 9, pp. 1443–1450, Sep. 2023.

[18] D. Sipal, M. P. Abegaonkar, and S. K. Koul, "Easily extendable compact planar UWB MIMO antenna array," *IEEE Antennas Wireless Propag. Lett.*, vol. 16, pp. 2328–2331, 2017.

[19] W. He, Y. He, Y. Li, S.-W. Wong, and L. Zhu, "A compact ultrawideband circularly polarized antenna array with shared partial patches," *IEEE Antennas Wireless Propag. Lett.*, vol. 20, pp. 2280–2284, 2021.

[20] V. Sipal, M. John, D. Neirynck, M. McLaughlin, and M. Ammann, "Advent of practical UWB localization: (R)Evolution in UWB antenna research," in *Proc. 8th Eur. Conf. Antennas Propag. (EuCAP)*, Apr. 2014, pp. 1561–1565.

[21] J. Jocqué, Q. Van den Brande, S. Luchie, B. Van Herbruggen, E. De Poorter, J. Verhaevert, S. Lemey, P. Van Torre, and H. Rogier, "Resource-efficient simulation framework for accurate UWB antenna system design," *IEEE Internet Things J.*, vol. 12, no. 9, pp. 11441–11456, May 2025.

[22] I. L. de Paula, S. Lemey, D. Bosman, Q. V. d. Brande, O. Caytan, J. Lambrecht, M. Cauwe, G. Torfs, and H. Rogier, "Cost-effective high-performance air-filled SIW antenna array for the global 5G 26 GHz and 28 GHz bands," *IEEE Antennas Wireless Propag. Lett.*, vol. 20, pp. 194–198, 2021.
[23] Q. Van den Brande, S. Lemey, J. Vanfleteren, and H. Rogier, "Highly efficient impulse-radio ultra-wideband cavity-backed slot antenna in stacked air-filled substrate integrated waveguide technology," *IEEE Trans. Antennas Propag.*, vol. 66, no. 5, pp. 2199–2209, May 2018.
[24] N. Claus, J. Verhaevert, and H. Rogier, "High-performance air-filled multiband antenna for seamless integration into smart surfaces," *IEEE Antennas Wireless Propag. Lett.*, vol. 20, pp. 2260–2264, 2021.
[25] G.-J. Gordebeke, S. Lemey, O. Caytan, M. Boes, J. Jocqué, S. Van de Velde, C. Marshall, E. De Poorter, and H. Rogier, "Time-domain-optimized antenna array for high-precision IR-UWB localization in harsh urban shipping environments," *IEEE Sensors J.*, vol. 24, no. 5, pp. 5561–5577, Mar. 2024.
[26] Y. Asci, "Wideband and stable-gain cavity-backed slot antenna with inner cavity walls and baffle for X- and Ku-band applications," *IEEE Trans. Antennas Propag.*, vol. 71, no. 4, pp. 3689–3694, Apr. 2023.
[27] K. Y. Kapusuz, S. Lemey, A. Petrocchi, P. Demeester, D. Schreurs, and H. Rogier, "Polarization reconfigurable air-filled substrate integrated waveguide cavity-backed slot antenna," *IEEE Access*, vol. 7, pp. 102628–102643, 2019.
[28] P. Liu, L. Chang, Y. Li, Z. Zhang, S. Wang, and Z. Feng, "A millimeter-Wave micromachined air-filled slot antenna fed by patch," *IEEE Trans. Compon., Packag., Manuf. Technol.*, vol. 7, no. 10, pp. 1683–1690, Oct. 2017.
[29] L. Van Messem, S. Sinha, I. Ocket, H. Trischler, E. Schlaffer, D. Schlick, H. Rogier, and S. Lemey, "Air-filled SIW technology for mass-manufacturable and energy-efficient terahertz systems," *Sci. Rep.*, vol. 13, no. 1, p. 16714, Oct. 2023.
[30] N. Yan, K. Ma, and H. Zhang, "A novel self-packaged substrate integrated suspended line quasi-yagi antenna," *IEEE Trans. Compon., Packag., Manuf. Technol.*, vol. 6, no. 8, pp. 1261–1267, Aug. 2016.
[31] *IEEE Standard for Low-Rate Wireless Networks*, Standard 802.15.4-2024, 2024.
[32] C.-Y. Chiu, P.-L. Teng, and K.-L. Wong, "Shorted, folded planar monopole antenna for dual-band mobile phone," *Electron. Lett.*, vol. 39, no. 18, pp. 1301–1302, Sep. 2003.
[33] P.-S. Chen, S.-C. Lin, T.-W. Chiu, and F.-R. Hsiao, "Surface-mount metal chip antenna with symmetric structure for WLAN application," in *Proc. TENCON-IEEE Region 10 Conf.*, Oct. 2007, pp. 1–3.
[34] D. L. H. Tong, P. Minard, P.-M. Morin, and J.-M. Le Foulgoc, "Stamped metal antenna including a feeding transmission line," in *IEEE MTT-S Int. Microw. Symp. Dig.*, May 2015, pp. 1–4.
[35] Antenna Datasheet. (2022). *AN01ML27M00 Series, JAE (Japan Aviation Electronics Industry)*. Accessed: Dec. 21, 2024. [Online]. Available: https://www.jae.com/en/antenna/an01
[36] KYOCERA AVX. (2022). *Wi-Fi 6 & Wi-Fi 6E or CBRS/n78 Stamped Metal Embedded Antenna*. Accessed: Dec. 21, 2024. [Online]. Available: https://www.kyocera-avx.com/product/wifibluetooth-stamped-metal-embedded-antenna-1000146/
[37] TE Connectivity. (2022). *Stamped MetalWiFi 6/6E Antenna*. Accessed: Dec. 21, 2024. [Online]. Available: https://www.te.com/usa-en/product-ANT-W63-MSA-TH1.html
[38] J. Park, D. Choi, and W. Hong, "Millimeter-wave phased-array antenna-in-package (AiP) using stamped metal process for enhanced heat dissipation," *IEEE Antennas Wireless Propag. Lett.*, vol. 18, pp. 2355–2359, 2019.
[39] S. Chen and H. H. Liu, "UWB slot antenna on shielding can for high accuracy positioning application," in *Proc. Global Congr. Electr. Eng. (GC-ElecEng)*, Sep. 2020, pp. 43–45.
[40] Q. V. d. Brande, S. Lemey, and H. Rogier, "Planar sectoral antenna for IR-UWB localization with minimal range estimation biasing," *IEEE Antennas Wireless Propag. Lett.*, vol. 20, pp. 135–139, 2021.
[41] Plug pin 1.0 mm for PCBs, 9.5 mm long, tin-plated, Vogt, datasheet. Accessed: Dec. 21, 2024. https://www.buerklin.com/en/p/vogt/pins/1364a-68/07F802/#downloads
[42] CST Studio Suite. (2022). *Dassault Systémes*. [Online]. Available: https://www.3ds.com/products-services/simulia/products/cst-studio-suite/
[43] (2019). *Southwest Microwave*. Accessed: Dec. 21, 2024. [Online]. Available: https://mpd.southwestmicrowave.com/product/10359-002j-2-92mmk- jack-female-bolt-on-vertical-launch/
[44] (2022). *Absorptive Coaxial SP3T Switch*. Accessed: Dec. 21, 2024. [Online]. Available: https://www.rflambda.com/pdf/switchers/RFSP3TA0118G.pdf
[45] T. T. Vo, L. Ouvry, A. Sibille, and S. Bories, "Mutual coupling modeling and calibration in antenna arrays for AOA estimation," in *Proc. 2nd URSI Atlantic Radio Sci. Meeting (AT-RASC)*, May 2018, pp. 1–4.

GERT-JAN GORDEBEKE (Member, IEEE) received the B.Sc. and M.Sc. degrees in electrical engineering from Ghent University, Ghent, Belgium, in 2015 and 2017, respectively. He is currently pursuing the Ph.D. degree with the IDLab-Electromagnetics Group, Department of Information Technology, IMEC, Ghent University. His current research interest includes robust multi-antenna ultra-wideband systems for high-precision localization.

SAM LEMEY (Member, IEEE) received the M.Sc. degree in electronic engineering from Howest University College West Flanders, Kortrijk, Belgium, in 2012, and the Ph.D. degree in electrical engineering from Ghent University, Ghent, Belgium, in 2016.

From January to March 2018, he was a Visiting Scientist with the Terahertz Photonics Group, Institute of Electronics, Microelectronics and Nanotechnology (IEMN), University Lille Nord de France, Lille, France. He is currently a Professor with the Department of Information Technology (INTEC), IMEC, Ghent University. His research interests include antenna systems for wearable applications, active antenna design for the Internet of Things and (beyond) 5G applications, (opto-electronic) millimeter-wave multi-antenna systems, impulse-radio ultra-wideband antenna systems for joint communication and sensing, and full-wave/circuit co-optimization frameworks to realize (opto-electronic) active (multi-)antenna systems.

Dr. Lemey received the URSI Young Scientist Award at the 2020 URSI General Assembly and the Best Paper Award at the 2016 IEEE MTT-S Topical Conference on Wireless Sensors and Sensor Networks. He was also a co-recipient of the 2015 Best Paper Award at the 22nd IEEE Symposium on Communications and Vehicular Technology in Benelux and the 2019 ECOC Best Demo Award.

HENDRIK ROGIER (Senior Member, IEEE) received the M.Sc. and Ph.D. degrees in electrical engineering from Ghent University, Ghent, Belgium, in 1994 and 1999, respectively.

From 2003 to 2004, he was a Visiting Scientist with the Mobile Communications Group, Vienna University of Technology, Vienna, Austria. He is currently a Senior Full Professor with the Department of Information Technology, Ghent University, and a Guest Professor with the Interuniversity Microelectronics Centre, Ghent. He has authored or co-authored over 210 articles in international journals and over 240 contributions in conference proceedings. His current research interests include antenna systems, radio wave propagation, body-centric communication, numerical electromagnetics, electromagnetic compatibility, and power/signal integrity. He is a member of the MTT TC-26 RFID, Wireless Sensor and IoT Committee, and AP-S TC-11 Health and Medicine. From 2017 to 2019, he was an Associate Editor of IEEE TRANSACTIONS ON MICROWAVE THEORY AND TECHNIQUES. He is an Associate Editor of *IET Electronics Letters* and *IET Microwaves, Antennas and Propagation*. He acts as the URSI Commission B representative for Belgium.